



Arabian Sea high salinity core supplies oxygen to the Bay of Bengal

Anoop A. Nayak^a, P.N. Vinayachandran^{a,b}, Jenson V. George^{a,1}

^a Centre for Atmospheric and Oceanic Sciences, Indian Institute of Science, Bengaluru, 560012, Karnataka, India

^b Divecha Centre for Climate Change, Indian Institute of Science, Bengaluru, 560012, Karnataka, India

ARTICLE INFO

Dataset link: <https://doi.org/10.5281/zenodo.7340408>, <https://dataselection.euro-argo.eu/>

Keywords:

Bay of Bengal oxygen minimum zone
Turbulence and salt fingering
Dissolved oxygen
BoBBLE and Argo data

ABSTRACT

The oxygen minimum zone (OMZ) in the Bay of Bengal (BoB) is unique owing to its curious capability to maintain steady dissolved oxygen (DO) levels. In this study, we identify a process by which the oxygen is supplied to the BoB, using DO and microstructure profiles in the southern BoB and Argo profiles over the entire basin. A high salinity core (HSC) rich in DO is advected by the Summer Monsoon Current (SMC) into BoB. Vertical mixing driven by turbulent processes recharge DO concentration in thermocline above OMZ. Salt-fingering processes were active below the HSC and were observed to enhance the vertical mixing. HSC identified in the Argo data, also rich in oxygen, can be traced up to 19° N, confirming that HSC is a source of DO and potentially prevents OMZ from moving to the denitrification regime. This might be a potential oxygen source for the BoB OMZ in changing climate conditions.

1. Introduction

Oxygen minimum zone (OMZ) is a region in the ocean interior where consumption of dissolved oxygen (DO) is greater than supply (Paulmier and Ruiz-Pino, 2009). Mixing of oxygen from the atmosphere and oxygen released in photosynthesis by phytoplankton modulate near-surface concentrations of DO. Below the surface, large-scale ocean circulation and vertical mixing are dominant physical processes that control oxygen levels (Wyrki, 1962; Sarma, 2002; Jain et al., 2017). The structure of OMZ in the world oceans has two primary controlling factors. Circulation in basins determines the extent of OMZ, whereas biological processes inside OMZ determine oxygen levels (Sverdrup, 1938; Wyrki, 1962; Vinayachandran et al., 2021). The northern basins of the Indian Ocean - the Arabian Sea (AS) and the Bay of Bengal (BoB) host some of the biggest OMZs amongst world oceans (Laffoley and Baxter, 2019; Rixen et al., 2020). BoB OMZ is the fourth largest in world ocean basins (Johnson et al., 2019), with the lowest DO levels at the northern edge (D'Asaro et al., 2020).

OMZs are the major contributors to the loss of fixed nitrogen in the ocean and this loss of fixed nitrogen in the ocean is due to the process called denitrification (Gruber and Sarmiento, 1997). All the major world ocean OMZs show active denitrification except the BoB (Howell et al., 1997; Bristow et al., 2017). Moreover, oxygen levels within OMZs in world oceans are decreasing (deoxygenation) due to global warming (Keeling and Garcia, 2002; Oschlies et al., 2018; Breitburg et al., 2018). Deoxygenation intensifies denitrification and results in

an increase in nitrogen release (Stramma et al., 2008). Deoxygenation trends in BoB are weak (Brandt et al., 2015; Laffoley and Baxter, 2019; Lachkar, 2020). DO levels within BoB OMZ are above a threshold, below which prolonged low DO values will trigger large-scale denitrification (Sarma et al., 2016; Bristow et al., 2017; Johnson et al., 2019). DO is suboxic in BoB OMZ but close enough to the threshold that its further decrease can initiate large-scale denitrification (Bristow et al., 2017; D'Asaro et al., 2020). The sources of oxygen or the processes by which oxygen levels are maintained above the threshold (tipping point) remain to be identified.

Denitrification is activated after the available DO levels drop below 6 $\mu\text{mol kg}^{-1}$ (Rixen et al., 2020) and the absence of large-scale denitrification in the BoB is because there is a supply of oxygen into the BoB OMZ. Supply of oxygenated water by anticyclonic eddies has been proposed as a plausible mechanism for supplying oxygen to the OMZ (Sarma and Udaya Bhaskar, 2018; Sarma et al., 2018; Johnson et al., 2019). But equally, in contrast, the cyclonic eddies are responsible for increased productivity and therefore increasing the oxygen demand (Kumar et al. (2007), Singh et al. (2015), Sarma et al. (2018). Demineralization depths in the BoB are higher than those in the Arabian Sea because of the larger and heavier mineral particles that BoB receives from huge river discharges (Rao et al., 1994; Le Moigne et al., 2013). The organic matter sinks with these heavier, larger mineral particles to the deeper ocean (higher demineralization depth) reducing its respiration rate and decreasing the oxygen demand in mid-level depths where OMZ is situated. This is responsible for the contrasts

* Corresponding author.

E-mail address: anoopn@alum.iisc.ac.in (A.A. Nayak).

¹ Current affiliation: National Centre for Polar and Ocean Research, Goa, 403804, India.

<https://doi.org/10.1016/j.dsr2.2025.105477>

Available online 18 March 2025

0967-0645/© 2025 Elsevier Ltd. All rights reserved, including those for text and data mining, AI training, and similar technologies.

in OMZs in the AS and the BoB (Al Azhar et al., 2017). However, several studies suggest the flow of oxygenated water masses as an efficient mechanism (Sarma, 2002; McCreary Jr. et al., 2013; Bristow et al., 2017; Sarma and Udaya Bhaskar, 2018). Using model experiments, it was suggested that the oxygen supply to layers above OMZ is essential for maintaining the DO concentrations within OMZ (McCreary Jr. et al., 2013).

The Summer monsoon current (SMC) has been well identified as the main pathway for transporting AS high salinity water to the BoB during boreal summer (Vinayachandran et al., 1999; Jensen, 2001; Webber et al., 2018). AS water forms the near-surface water over the AS basin and subducts below the warm, fresher near-surface BoB water as a high salinity core (HSC). HSC advected by SMC to the southern BoB, mixes with the ambient BoB waters as it moves northward; there is evidence of HSC as north as 12° N (Gordon et al., 2017; Jain et al., 2017). SMC intermittently supplies oxygen-rich Persian Gulf water to the BoB OMZ (Sheehan et al., 2020). Although the flow of oxygen-rich water along with SMC in southern BoB has been identified as the essential conduit for the supply chain, the process of oxygenation of BoB water has not been identified.

In this study, we used *in situ* dissolved oxygen and microstructure profiles to show fluxes of DO from the HSC into ambient water in the southern BoB. Argo float profiles across the BoB basin are used to understand the spread of high-salinity water and its implications for the distribution of DO.

2. Data and methods

2.1. BoBBLE ADCP, CTD, and VMP

In situ profiles were collected during the Bay of Bengal Boundary Layer Experiment (BoBBLE) from 25 June 2016 to 24 July 2016 (Vinayachandran et al., 2018; Fig. 1). The measurements included a time series station (TSE) from 4 July 2016 to 14 July 2016 at 89° E, 8° N. A section was occupied twice, along 8° N from 85.3° E to 89° E. Continuous current measurements were carried out using a hull-mounted 150 kHz Teledyne RDI Ocean Surveyor Acoustic Doppler Current Profiler or ADCP. The vertical resolution was 2 m, and single ping data were at 8-s intervals. Before calculating gradients of ADCP currents, a 1-h moving average was applied along time and a 4-m moving average along the vertical direction to remove high-frequency noise. The choice of 4-m was consistent with the 8-s slots used for microstructure estimates.

A factory-calibrated SeaBird Electronics (SBE) 9/11 + Conductivity–Temperature–Depth profiler (CTD) was used for measuring vertical profiles of temperature, salinity, and DO. 12 Niskin Sampler bottles of 10 L each on a Rosette Frame were used to collect water samples at discrete depths to measure various biogeochemical parameters. Analysis of dissolved oxygen (DO) at a precision of $\pm 0.03 \mu\text{M}$ was based on modifying the traditional Modified Winkler titration (Carpenter, 1965). These DO data sets were used to calibrate the CTD measurements of DO. There was significant agreement between Winkler DO and CTD DO with the coefficient of determination ($r = 0.99$, $n = 306$, $p < 0.01$). Isothermal layer depth (ILD) is defined as the depth with a 0.8 °C decrease compared to sea surface temperature (George et al., 2019). The depth below which density exceeds near-surface value by an increment due to 0.8 °C reduction in temperature is considered the mixed layer depth or MLD (Kara et al., 2000).

Microstructure profiles were collected at CTD stations using a vertical microstructure profiler (VMP — make Rockland Scientific). VMP had two airfoil shear sensors and one FP07 temperature sensor, which measured microstructure shear and temperature gradients with a sampling rate of 512 Hz. CT sensors (JFE Advantech, sampling rate of 64 Hz) measured accurate temperature and salinity. The top 10 m of the microstructure observations were ignored to avoid contamination from disturbances from ship proximity. The shear and temperature gradient

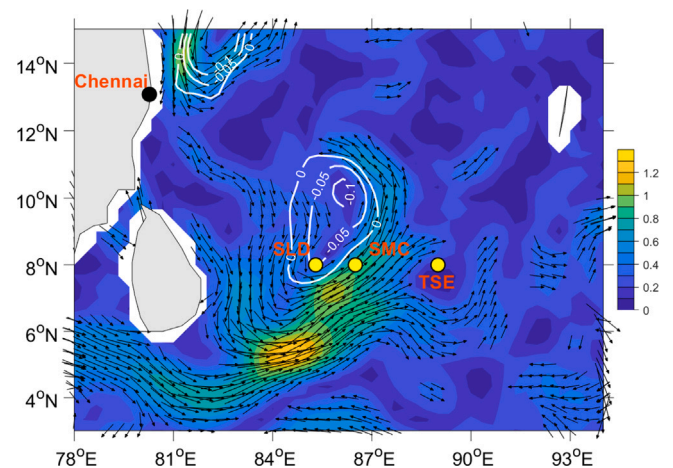


Fig. 1. Locations of stations within SLD, SMC, and at TSE. SLD stations were the westernmost stations in BoBBLE. A time series station was located at TSE (89° E, 8° N), the easternmost of the stations. SMC stations were aligned across the strong northeastward currents. Fig. 1 of Nayak et al. (2022) shows the exact locations of several stations counted as SLD and SMC stations during BoBBLE. Chennai was the point of the port. Vectors (for speeds $> 0.3 \text{ m s}^{-1}$) and colour (m s^{-1}) are current vectors and magnitude, respectively, at the start of the BoBBLE mission, end of June 2016. White contours show negative Sea Surface Height Anomalies (SSHA, m), manifesting the SLD. Currents from Ocean Surface Currents Analyses Real Time (OSCAR) datasets and SSHA from Copernicus Climate Change Service.

microstructure from VMP were used to estimate dissipation rates of turbulent kinetic energy (ϵ) and temperature variance (χ) (Bluteau et al., 2011, 2017). The shear and temperature gradient microstructure profiles were segmented (8-s; approximately 4-m of data for average fall speed of VMP $\sim 0.5 \text{ m s}^{-1}$) in the vertical, and each segment is used to calculate spectra of the temperature gradient. Integral and spectral fitting methods were applied over each segment of temperature gradient microstructure to estimate χ corresponding to ϵ (Bluteau et al., 2017). 2–3 microstructure profiles were collected within an hour during a single VMP operation. VMP operations were roughly at 5.5-h intervals during the time series.

Coefficients of turbulent diffusivity of density (K_ρ) and heat (K_T) were obtained from the estimates of ϵ , χ , background stratification and background temperature gradient (Osborn and Cox, 1972; Gregg, 1973; Osborn, 1980) using the expressions:

$$K_\rho = \Gamma \frac{\epsilon}{N^2}; \quad K_T = \frac{1}{2} \frac{\chi}{(\nabla T)^2} \quad (1)$$

Where, N^2 is Brunt–Väisälä frequency, ∇T is background gradient in temperature, and Γ is the mixing ratio. For oceanographic applications, Γ is widely considered constant and equal to 0.2 (St. Laurent and Schmitt, 1999; Gregg et al., 2018). We have estimated Γ_{obs} from our *in situ* observations using the formula $\Gamma_{obs} = [0.5N^2\chi] / \left[\epsilon \left(\frac{dT}{dz} \right)^2 \right]$ (Oakey, 1985; Hamilton et al., 1989) and Fig. 2 shows distributions of estimates of Γ_{obs} within the high salinity core, belonging to different mixing regimes. Fig. 3 shows the mean values of Γ_{obs} in each regime. The error bars shown in Fig. 3 are calculated using the propagation of errors from each parameter in the expression for Γ_{obs} (St. Laurent and Schmitt, 1999). The values Γ_{obs} are lower for the doubly-stable (DS) regime than that in the salt fingering (SF) regime. Considering the *in situ* values of Γ_{obs} in the doubly stable regime, we have used a higher value of $\Gamma = 0.27$ for the calculation of K_ρ . This is an average Γ_{obs} in the doubly stable regime.

Turner angle (Tu) is a measure of identifying possible sites for double-diffusive convection and salt fingering processes (Ruddick, 1983). It is calculated as $Tu = \tan^{-1} \left(\frac{N_T^2 - N_S^2}{N_T^2 + N_S^2} \right)$ (in degrees). Here N_T^2 and N_S^2 are contributions of temperature and salinity to N^2 respectively

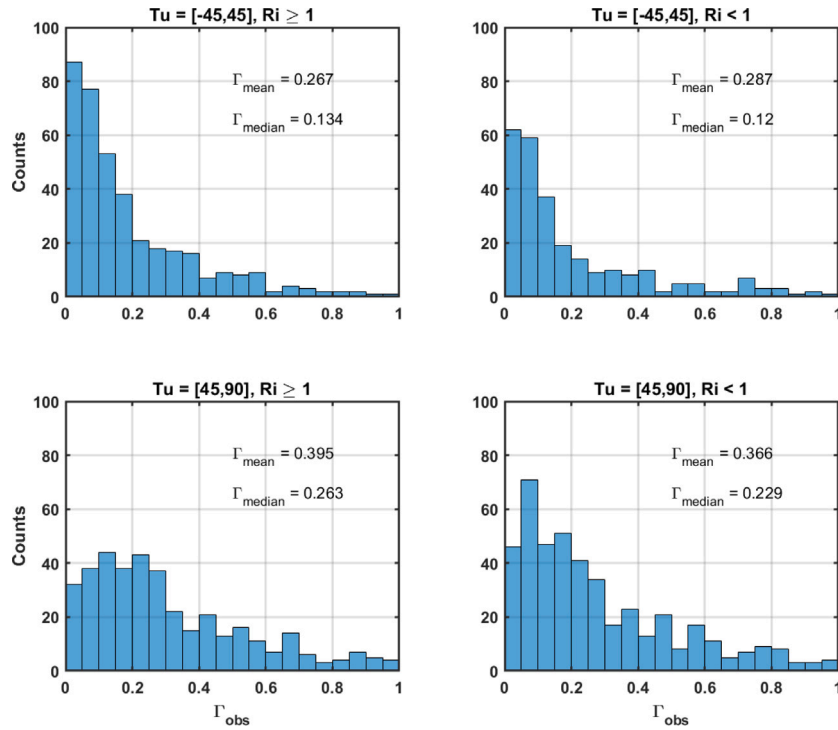


Fig. 2. Γ_{obs} distribution is shown for four regimes (based on the values of Tu and Ri). Two panels on the top show Γ_{obs} distribution for the doubly-stable regime ($-45^\circ < Tu < 45^\circ$). The bottom two panels show Γ_{obs} for salt fingering regime ($45^\circ < Tu < 90^\circ$). The first column shows $Ri \geq 1$ and the second for $Ri < 1$. Mean and median values of Γ_{obs} are shown on the top right of each panel. In turbulent regimes, the Γ values are lower than that in the salt-fingering regime. [Richardson number, $Ri = N^2 / ((\partial u / \partial z)^2 + (\partial v / \partial z)^2)$].

(George et al., 2021). Tu values in between (45,90) degrees suggest the presence of salt fingering processes, and Tu in between ($-45,45$) degrees suggest a doubly-stable regime. Γ is also considered to distinguish sites for salt fingering (George et al., 2021). The parameters discussed in this paragraph are calculated using the temperature and salinity profiles obtained from the 64 Hz CT sensors on VMP. A 4-m moving mean (corresponding to the 4-m binning for estimation of dissipation rates) is applied along the vertical before calculating the parameters.

Tracer diffusion from HSC in the southern Bay of Bengal (BoB) to ambient water can occur by turbulent and double-diffusive processes (George et al., 2019, 2021). Since the HSC observed across the measurements was warmer than ambient water, some locations were active in salt fingering, and this process enhanced diffusivity (George et al., 2021). If $\Gamma_{obs} > 0.3$ and $45 < Tu < 90$ then eddy diffusivity due to salt fingering is modelled as $K_{SF} = R_\rho K_T / \gamma$ (St. Laurent and Schmitt, 1999) where R_ρ (density ratio) = $\alpha(\frac{dT}{dz}) / \beta(\frac{dS}{dz})$ and γ (flux ratio) is considered equal to 0.7 (Fernández-Castro et al., 2014; George et al., 2021). This method gives diffusivity profiles at all VMP stations, including turbulent and salt-fingering processes. In the estimation of K_ρ , K_T , and K_{SF} the denominator place of each expression consists of gradients of density (in the form of N^2), temperature, and salinity (in the form of N_S^2), respectively. A lower limit of each term (the gradients) is used to avoid very low values inducing spikes in the derived quantities. N^2 and N_S^2 are limited to an absolute minimum value of 10^{-5} s^{-2} . The background gradient of temperature is limited to an absolute minimum value of $0.01 \text{ }^\circ\text{C m}^{-1}$. These limits are decided after looking at the raw distribution of each parameter and avoiding any points past 1% of the total number of points. Similarly, the square of the shear of currents obtained from ADCP profiles, used to estimate the local Richardson number, is limited to an absolute minimum value of 10^{-5} s^{-2} .

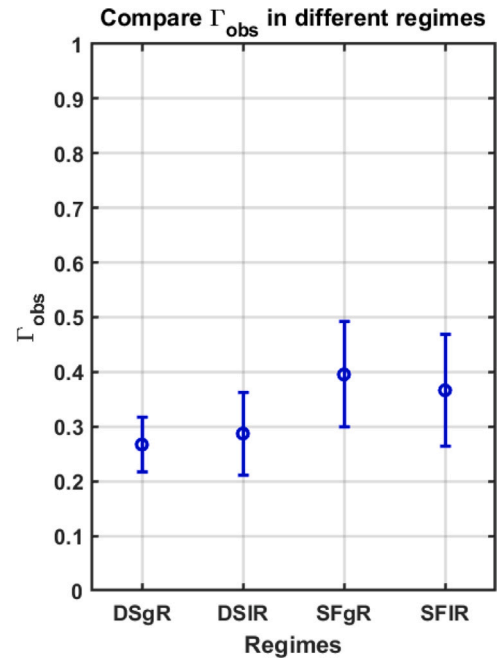


Fig. 3. Mean Γ_{obs} is shown for four regimes on the X-axis (based on the values of Tu and Ri). DSgR - $-45^\circ < Tu < 45^\circ$, $Ri \geq 1$; DSIR - $-45^\circ < Tu < 45^\circ$, $Ri < 1$; SFgR - $45^\circ < Tu < 90^\circ$, $Ri \geq 1$; SFIR - $45^\circ < Tu < 90^\circ$, $Ri < 1$. The first two points (from left) belong to a doubly stable (DS) regime, whereas the last two are in a salt-fingering (SF) regime. The highest mixing ratio is observed in a purely salt-fingering regime when $Ri \geq 1$ (SFgR). The mixing ratio decreases in the salt-fingering regime when $Ri < 1$ (SFIR).

2.2. Calculation of DO flux

If simultaneous profiles of oxygen and diapycnal diffusivity values are available, diapycnal oxygen flux (F_{DO}) can be estimated using Fick's law of diffusion (Sharples et al., 2003; Fischer et al., 2013; Brandt et al., 2015) as follows:

$$F_{DO} = -\rho K_{oxy} \frac{\partial DO}{\partial z} \quad (2)$$

In Eq. (2), ρ is the density of water, K_{oxy} is the diapycnal diffusivity of DO. Estimates of K_{oxy} were obtained from VMP. If salt fingering is indicated at any depth, then $K_{oxy} = R_{\rho} K_T / \gamma$ (St. Laurent and Schmitt, 1999; George et al., 2021). R_{ρ} and γ are density ratio and flux ratio, respectively. If salt fingering is not indicated, then $K_{oxy} = K_{\rho}$ (Fischer et al., 2013). $\frac{\partial DO}{\partial z}$ in Eq. (2) is the DO gradient obtained from DO profiles. K_{oxy} and $\frac{\partial DO}{\partial z}$ in Eq. (2) require that they are estimated from simultaneous measurements (Fischer et al., 2013). In contrast, VMP and CTD operations were not concurrent, and there were differences in the times of VMP and closest CTD operations at a station.

Profiles of diffusivity and DO were corrected for alignment before using them in Eq. (2). We have considered the profile of DO from CTD operations whose time of operation was closest to the time of VMP operation for the estimation of F_{DO} . Once the closest DO profile is selected, DO values are picked up from the CTD profiles and interpolated to the corresponding density levels of diffusivity values for every diffusivity value in the vertical. For example, consider a diffusivity value at 100 m and density levels 2 m above and below this point. The DO values from the closest CTD profile are interpolated to these two density levels. The gradient of DO is calculated using these two DO values for the corresponding diffusivity value.

2.3. Argo profiles

To investigate the spread of oxygen-rich high salinity water into the BoB, we have used profiles from 249 Argo floats deployed between 2002–2021 spread across the BoB (Argo, 2000) (<https://argo.ucsd.edu>, <http://www.ocean-ops.org>, <http://dataselection.euro-argo.eu/>). The Argo data is available with flags for quality check. This study uses data flagged as 'good_data' or 'probably_good_data.' The Argo floats provide temperature and salinity profiles at 2 m resolution. Since the depth range of HSC is limited to the top 200 m, we have restricted the use of the Argo data in the top 200 m. All profiles from this collection with $20^{\circ}\text{C} \leq \theta$ (potential temperature) $\leq 27^{\circ}\text{C}$, and $S \geq 35$ psu within the top 200 m were considered for the analysis. These criteria helped identify Argo profiles with temperature–salinity characteristics of HSC captured during BoBBLE. Application of this criteria resulted in 2042 profiles to the north of 8°N in the BoB.

3. Results

The *in situ* observations captured characteristic dynamic features at their peak in the Southern BoB (Vinayachandran et al., 2018). Stations along the western edge of the 8°N section occupied during BoBBLE were within the seasonal cyclonic circulation called Sri Lanka dome or SLD (Vinayachandran and Yamagata, 1998). SLD is a cyclonic eddy that forms east of Sri Lanka during the southwest monsoon, and the SMC forms the eastern arm of the cyclonic circulation (Vinayachandran and Yamagata, 1998; Vos et al., 2014; Cullen and Shroyer, 2019). The wind stress curl over the region forces upwelling within the eddy resulting in the doming of the subsurface thermocline (Vinayachandran and Yamagata, 1998). Temperature contours in *in situ* observations shoaled to the westernmost stations along the sections, manifesting the impact of SLD (Fig. 4a and 4c). A time series station (TSE) was conducted at the eastern edge (at 8°N , 89°E) of the section (Fig. 1), and stations between section edges were across the core of SMC (Nayak et al., 2022). SMC, flowing northeastward to the east of SLD, is a source of high salinity Arabian Sea water. This is evident from the stations showing

a high salinity core with strong currents (Fig. 5a, 5c, 5d, and 5f). A subsurface high salinity core (HSC (Vinayachandran et al., 2013), $S > 35$ psu) was present at TSE and at the stations crossing SMC but not at the stations within SLD. HSC was thickest (~ 110 m) across the first 8°N section (Fig. 4d). At TSE (Fig. 4e), HSC thickness increased from (~ 20 m) at the start of the time series (4–7 July 2016) to ~ 90 m towards the end (14 July 2016). The TSE captured the evolution of HSC (Fig. 4e) with a layered structure in the currents (Fig. 5b and 5e).

3.1. Distribution of the diffusivity values

Diffusivities (K_{ρ} and K_{SF}) estimated using VMP measurements were divided into two layers within HSC to distinguish the processes at the top and bottom of the HSC. The top layer of HSC extends between the top 35 psu contour and the depth of maximum salinity. The bottom layer extends downwards from the depth of maximum salinity to double the distance between the depth of maximum salinity and the bottom 35 psu contour. The bottom layer is thicker to include the depths with high values of dissipation rates below the 35 psu contour as shown in George et al. (2019, 2021). The distribution of diffusivities is due to the effect of the background state on the generation of turbulent processes (Fig. 6). Due to reduced stratification in the bottom layer of HSC, turbulent events are more likely within the bottom layer of HSC than the top of HSC (Nayak et al., 2022). HSC was warmer than ambient water, which gave way to salt fingering processes at its bottom and enhanced diffusivities (George et al., 2021).

3.2. Dissolved oxygen

The observations captured temporal and spatial variation of DO at the stations (Fig. 7). Highest DO values ($\sim 185 \mu\text{mol kg}^{-1}$) were observed near the surface within ILD. Below ILD, DO contours followed salinity contours in the top 200 m. Depths of contours with lower DO ($\sim 50 \mu\text{mol kg}^{-1}$) increased with an increase in thickness of HSC in the subsurface (Roy et al., 2021). DO decreased from $150 \mu\text{mol kg}^{-1}$ at the top of HSC to $50 \mu\text{mol kg}^{-1}$ at the bottom (Fig. 7). The thickness of the oxycline (~ 50 – $150 \mu\text{mol kg}^{-1}$ layer) was lowest at stations within SLD where HSC was absent and comparatively high where HSC was present. Contours of lower DO ($< 50 \mu\text{mol kg}^{-1}$) were observed at depths shallower than 50 m at SLD stations (Roy et al., 2021) while they were deeper than the depth of the bottom of HSC at other stations. These figures suggest that HSC is a source of DO in the BoB.

3.3. DO fluxes

The turbulent and salt fingering processes mixed the DO from the HSC to the water layer below HSC. DO fluxes were generally directed downward since the DO values decreased with depth. DO fluxes within HSC were binned along the vertical in two layers separated at the depth of maximum salinity within the HSC. This is to distinguish between processes at the top and bottom of HSC (Section 3.1). Fig. 8 shows histograms of DO fluxes within the two layers. Figs. 8a and 8c show that the turbulent fluxes in the top layer concentrated to lower fluxes than the bottom layers of HSC. The median of turbulent fluxes in the top layer is lower than in the bottom. The average turbulent flux in the top layer is $9.363 \times 10^{-4} \mu\text{mol m}^{-2} \text{s}^{-1}$ and lower than that in the bottom layer, $0.0114 \mu\text{mol m}^{-2} \text{s}^{-1}$ which is one order of magnitude difference.

Salt fingering processes enhance the fluxes below the HSC (George et al., 2021). The salt-fingering DO fluxes of $O(10^{-2}$ – $10^{-1} \mu\text{mol m}^{-2} \text{s}^{-1})$ in the bottom layer were 1–1.5 orders of magnitude higher than the layer average turbulent fluxes (Fig. 8). The average DO flux due to salt fingering ($0.2996 \mu\text{mol m}^{-2} \text{s}^{-1}$) is approximately 30 times the magnitude of the average bottom layer turbulent fluxes. Average DO fluxes in the bottom layer were higher than in the top layer, suggesting that HSC loses more oxygen to the subsurface than it receives at its top

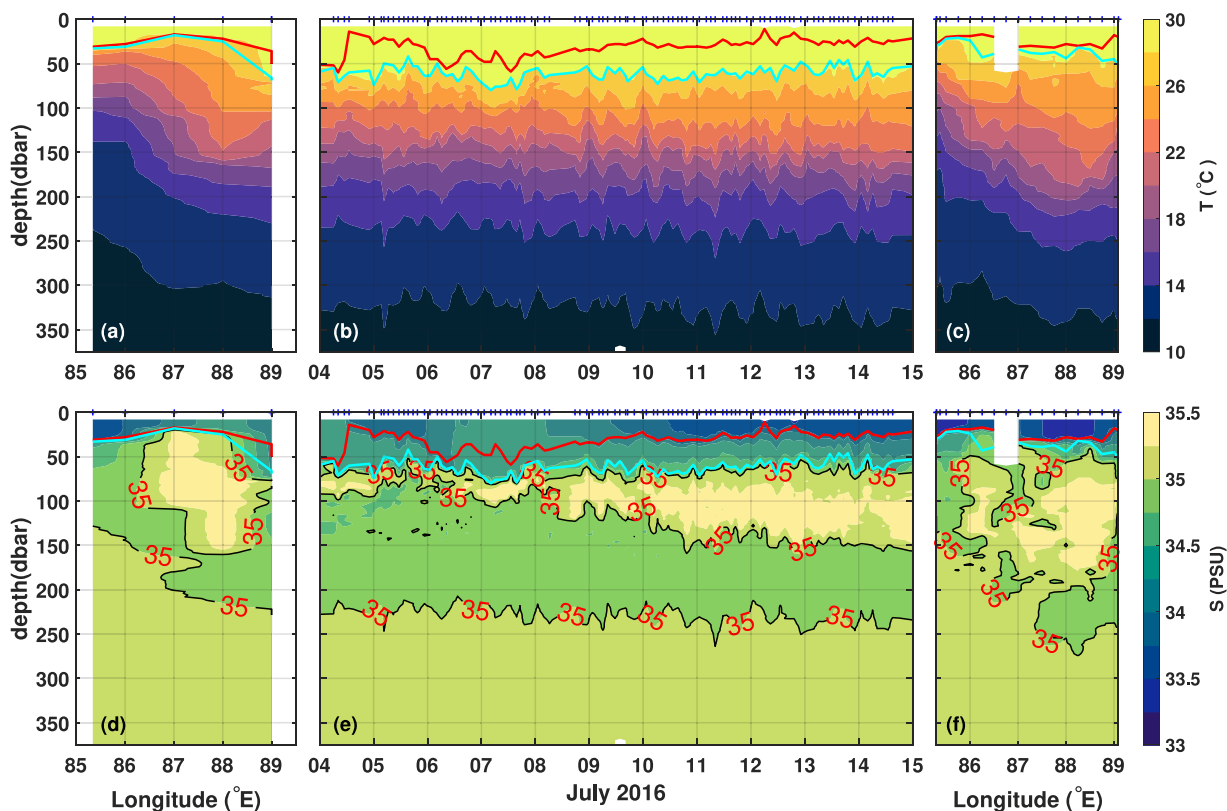


Fig. 4. Temperature (a)–(c) and Salinity (d)–(f) from BoBBLE. The first and last columns show the sections along 8° N latitude before and after the time series, respectively. The middle column shows the time series. Blue plus symbols on top show the location of CTD operation for the sections and times of CTD operations for the time series. Colorbars for respective parameters are shown to the right. Red and cyan lines show MLD and ILD, respectively. Temperature contours shoal towards the west in the sections suggest the effect of SLD. HSC was observed in sections and the time series.

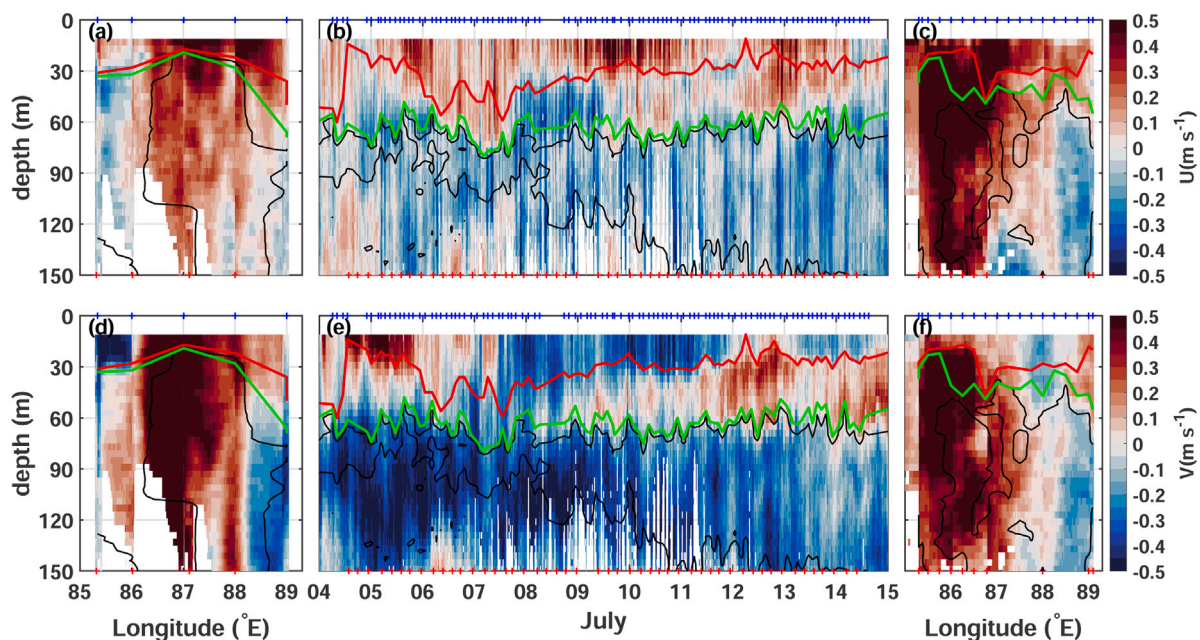


Fig. 5. ADCP current measurements from BoBBLE. The columns are arranged in the same way as in Fig. 4. (a)–(c) U and (d)–(f) V. Black contours show the 35 psu salinity contour. Red and green lines show MLD and ILD, respectively. Blue plus symbols on top show location of CTD operation for the sections and times of CTD operations for the time series. Similarly, red plus symbols at the bottom of the panels are for VMP operations. Strong northwesterward moving SMC and HSC captured in the sections.

from the mixed layer. The average fluxes are high in the bottom layer because of more events of higher-order diffusivity values than in the upper layer. Two orders of magnitude difference between the mean and

median of K_{SF} values within the bottom layer of HSC (Fig. 6) suggest that high flux processes are intermittent. To summarize, at the stations with HSC, there is a loss of DO to deeper layers.

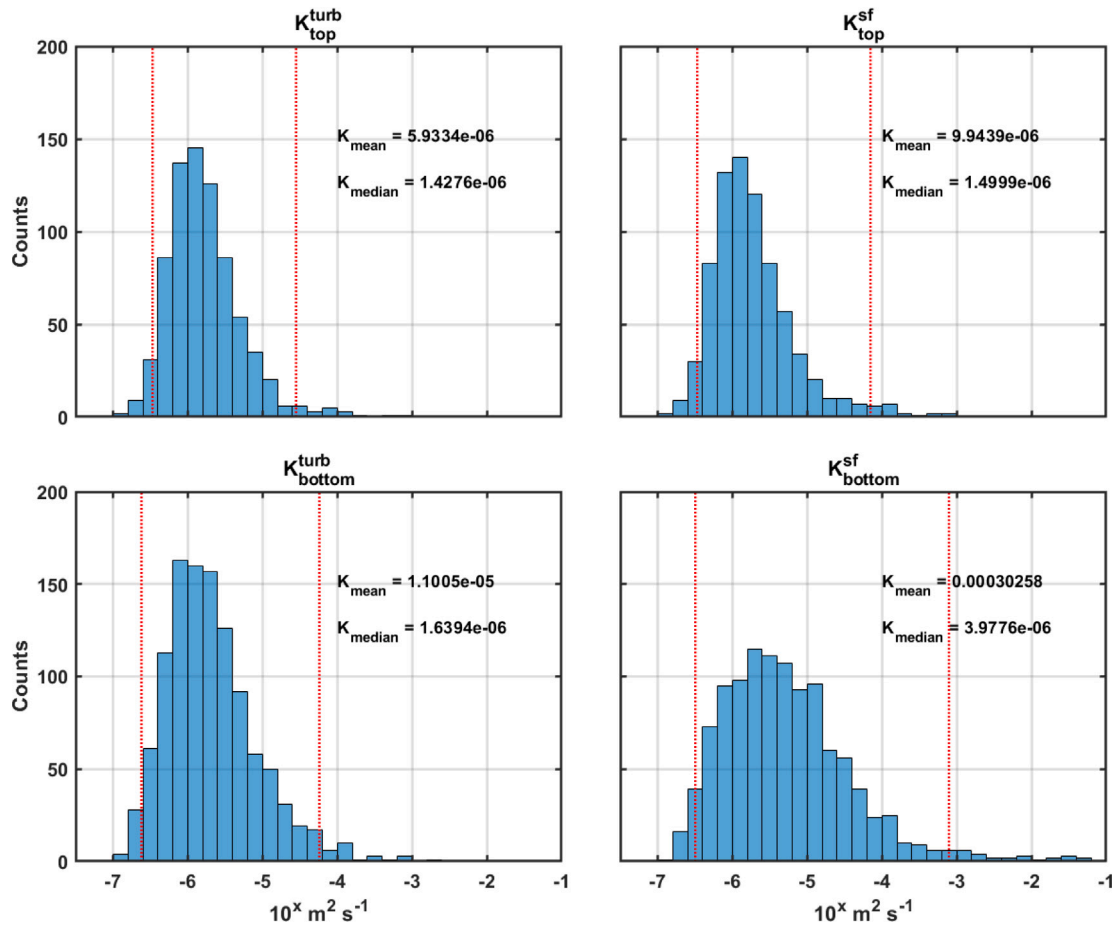


Fig. 6. The top rows are the distribution of K_p (left) and K_{SF} (right) in the top layer of HSC, and the bottom row shows the distribution of K_p (left) and K_{SF} (right) in the bottom layer of HSC. The distribution at the bottom right is skewed to higher diffusivity values due to salt fingering. Mean and median values (in $m^2 s^{-1}$) are shown at the top right of each window. Red dotted vertical lines capture 95% of the diffusivity values in each window.

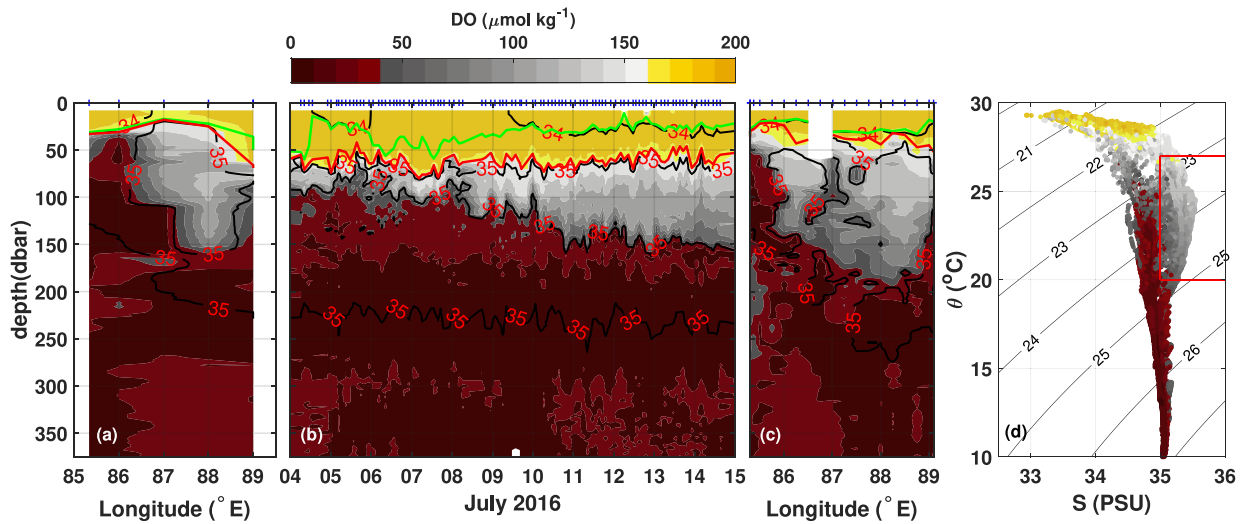


Fig. 7. BoBBLE observations of DO (a)–(c). The panels (a) and (c) are arranged in the same way as in Fig. 4. The Blue plus symbol on top shows the time of CTD operation in (b) and the location of CTD operation in (a) and (c). Thick black lines are salinity contours with one psu intervals. The red line is ILD, and the green line is MLD. (d) shows the θ -S diagram of BoBBLE observations. The colours of the scatter plot show the DO concentrations. The colorbar shown at the top of the figure is common to all. The red box in (d) wraps HSC characteristics ($S > 35$ psu; $20^\circ C < \theta < 27^\circ C$).

3.4. Spread of HSC using Argo data

The locations of Argo profiles selected based on the criteria described in Section 2.3 show the spread of HSC in the BoB (Fig. 9).

Argo profiles having HSC signatures are densely concentrated in the southern BoB (mostly between $86\text{--}88^\circ E$). Fig. 9b, 9c show locations and times of Argo profiles selected for the year 2016. The size of bullets increases with time in Fig. 9b, suggesting that HSC signatures

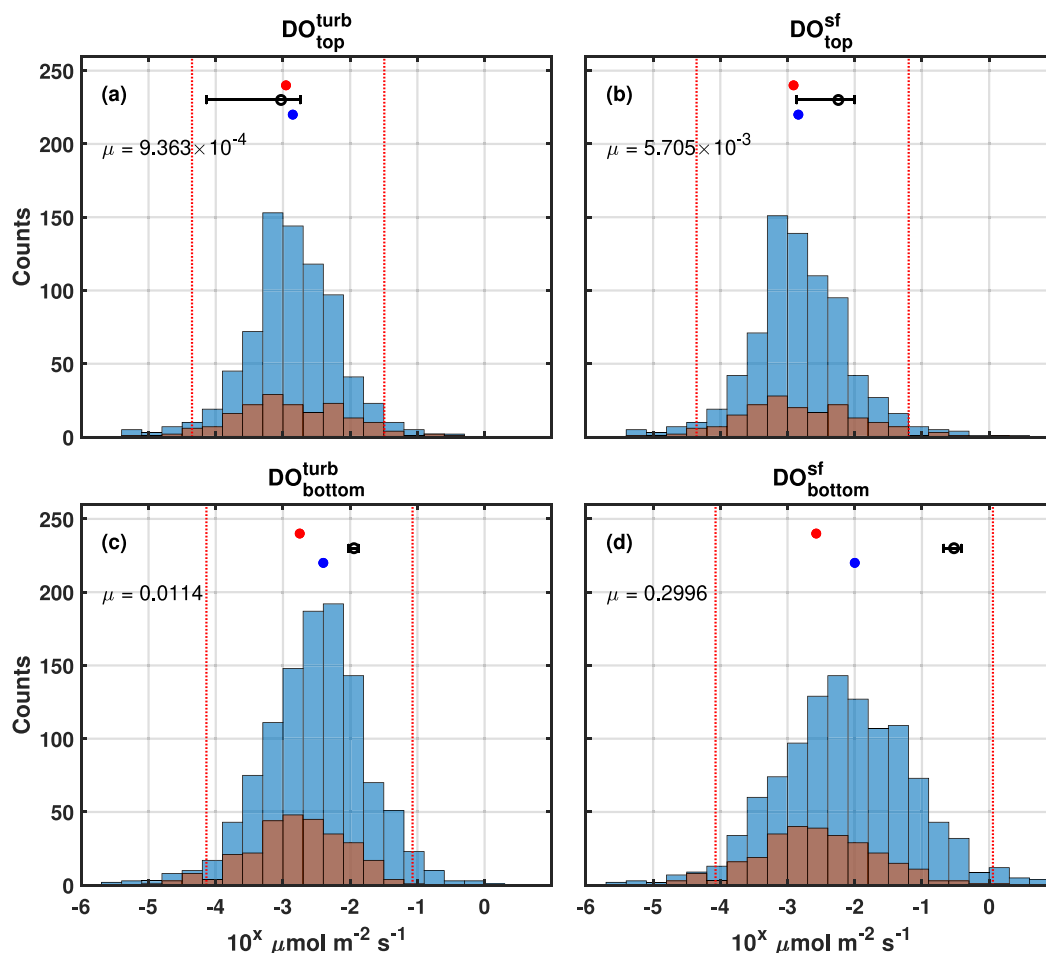


Fig. 8. Histograms of DO fluxes in two layers (top and bottom layers of HSC) and for two mechanisms — only turbulence (turb) and including salt fingering(sf). (a) and (b) show the distributions of DO flux for the top layer of HSC and (c) and (d) for the bottom layer. Blue-coloured bars are the DO fluxes directed upwards, and those in brown are DO fluxes directed downwards. The red dotted vertical lines capture 95% of all the observed fluxes in the layer. Blue and red-filled bullets on top mark the medians of downward and upward-directed fluxes, respectively. The X -axis shows $\log_{10}(\text{DO flux})$. The layer average of DO fluxes (μ) is mentioned on the top-left of each panel. Standard error with the mean is shown using a black error bar at the top of each panel. Each layer has a gross downward flux (positive μ).

spread through the BoB after entering the basin. The colours indicate a northward movement of HSC. Depths of maximum salinity of HSC identified at respective Argo locations (Fig. 9c) were within the range 50–150 m (also found in Gordon et al. (2016)). These depths are close to values shown in model simulations (Singh et al., 2022). Argo profiles suggest that high salinity Arabian Sea water enters the southern BoB and spreads in BoB along these depths. The decrease of salinity values in Fig. 9b suggests HSC mixing with ambient water as it moves northward.

A total of 79 Argo profiles with high salinity signatures north of 8°N between June–December of 2002–2021 had both salinity and DO profiles. Fig. 10 shows TS diagrams of the Argo profiles in three latitude ranges within the BoB. The most number of the profiles were observed in the range 10 – 14°N . Fig. 11 shows a finer decomposition of the number of profiles contributing to the histogram in Fig. 10e. The highest contribution from the available profiles is between 12 – 14°N . Although this distribution is dependent on the availability of Argo profiles in the region, it shows the propagation of HSC into the BoB. The SMC enters the southern BoB and its strongest currents advecting the HSC are limited to a maximum of 10°N (Rath et al., 2019). The presence of HSC north of the maximum extent of strong currents of SMC suggest that other circulation features within the basin move HSC further north in the BoB. The red boxes in Fig. 10a–c bound the same region in $\theta - S$ domain as shown in Fig. 7d. Since the Argo profiles are limited in number and non-uniform in basin coverage, tracking high salinity signatures is unreliable. However, Fig. 10 reveals that

HSC is present up to 15°N . These HSC signatures were present at depths shallower than 150 m, similar to results discussed in the BoBBLE observations (Fig. 7).

Fig. 7d shows that the high salinity water found in BoBBLE observations inside the box (based on θ and salinity criteria in Section 2) is within isopycnals 22.7 – 24.9 kg m^{-3} . DO values from the Argo profiles located within these isopycnals are separated into two categories based on the salinity criterion (Fig. 10d, 10e). If the DO values have corresponding salinity $> 35 \text{ psu}$, they are considered points *with HSC*. Else, DO values are considered as points *without HSC*. 7278 points were selected from 1382 profiles *without HSC* and 595 points were selected from 79 profiles *with HSC*. The mean and median DO from points *with HSC* were higher than the mean and median DO from points *without HSC*. The points *without HSC* are skewed to lower DO values (Fig. 10d) than the points *with HSC* (Fig. 10e). This difference in DO between *with HSC* and *without HSC* is the excess DO that HSC adds to the BoB. Oxygen-rich high salinity water spreads in BoB and mixes with BoB water between these isopycnals (Jain et al., 2017). The resultant water mixture between these isopycnals will be rich in DO. DO generally decreases from high ($\sim 180 \mu\text{mol kg}^{-1}$) values near the surface to low ($< 50 \mu\text{mol kg}^{-1}$) values below the surface. Fig. 10 suggests that this decreasing trend is slower for water columns with high salinity water. Therefore, high salinity water transports relatively higher DO and replenishes the deeper water with DO.

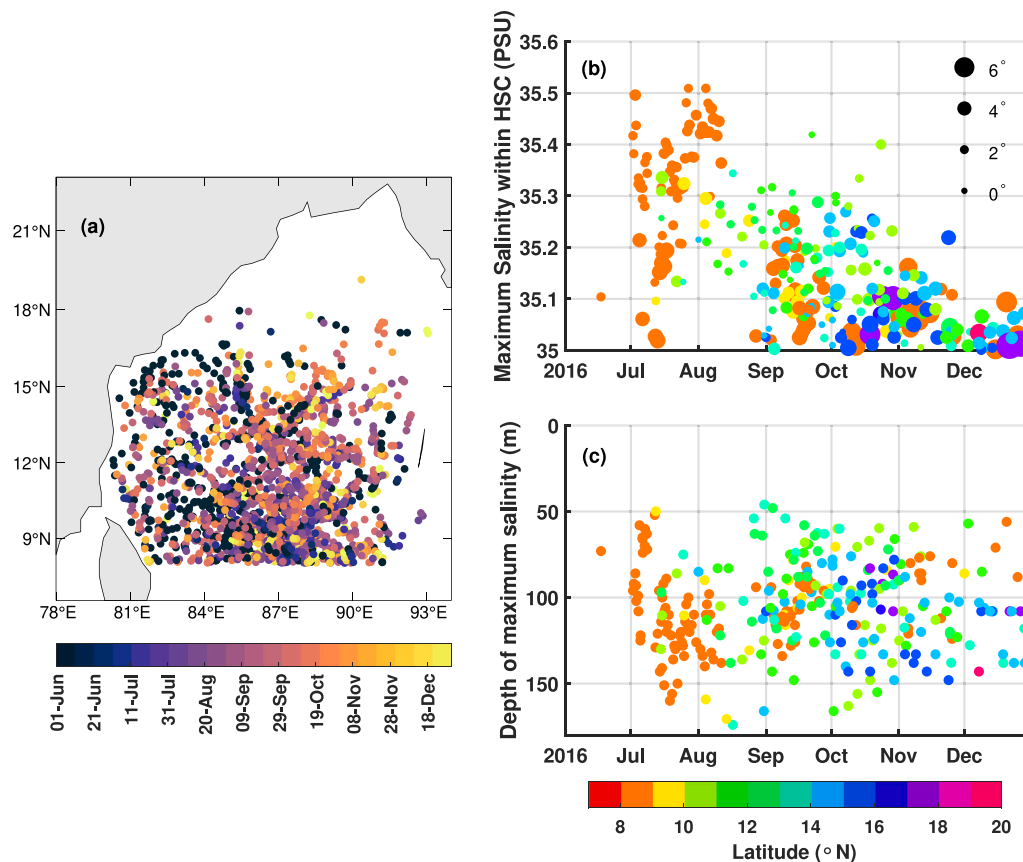


Fig. 9. (a) Locations of ArgO profiles with HSC signature. Near the 8° N latitude, profiles with HSC signatures were observed around the end of the year. Few profiles in the northern BoB (as far as 19° N) were obtained at the end of the corresponding year. (b) The Y-axis scales the maximum salinity value within the HSC found in the selected ArgO profiles from June to December 2016. The sizes of bullets are proportional to the distance (in degrees) of profile location from 85° E longitude (Black bullets provide sizes for distances in degrees). Maximum salinity decreased with an increase in latitude and time. (c) Y-axis shows the depth of maximum salinity varying between 50–150 m. The colours in (b) and (c) show latitude.

3.5. Transport of DO

The expression for oxygen supplied by the SMC into the BoB is $Q = (W \times H \times U \times \Delta t) \times (\rho_{AS} \times \Delta DO)$ (Sheehan et al., 2020). The product of quantities in the first bracket is the volume transported by SMC. Here, W is the width of SMC and is taken as 200 km (Fig. 7). H is the thickness of HSC, which loses salinity and DO to the bottom layers. We have taken $H \approx 50$ m. Current speed, $U \approx 0.5$ m s⁻¹ after considering currents within the top 150–200 m (Fig. 5). The effective transport of HSC at the southern BoB is assumed to last for a month, $\Delta t \approx 30$ days. The product in the second bracket is the excess DO per unit volume transported by SMC. Density (ρ_{AS}) ≈ 1023.5 kg m⁻³ since the ArgO profiles were considered based on the presence or absence of HSC within a layer between the isopycnals 22.7–24.9 kg m⁻³. ΔDO is difference of DO values between points with HSC and without HSC. Fig. 10 shows that the difference in median values of DO between points with HSC and without HSC is more than 25 $\mu\text{mol kg}^{-1}$. For the estimate here, we have assumed $\Delta DO = 20$ $\mu\text{mol kg}^{-1}$. This is to the lower side of the difference of medians, considering the bias due to the high density of floats identified in the southern BoB. These values estimate $Q = 2.65 \times 10^{17}$ μmol .

The estimate, Q is the excess DO that SMC transports to the layer between the isopycnals mentioned. Assuming the basin size of 1000 km \times 1000 km and the layer thickness as 120 m, the total increase in the DO is 2.15 $\mu\text{mol kg}^{-1}$. The actual basin area covered by the high salinity water is lesser depending on the circulation within the basin Sheehan et al. (2020). However, Fig. 9a and 9b show the spread of HSC in the BoB and suggest that HSC is a source of salinity and DO throughout the basin with time. The estimate Q is an order of magnitude higher than

that estimated for Persian Gulf influx (Sheehan et al., 2020) because the AS water has a larger volume than the Persian Gulf water (Jain et al., 2017; Sheehan et al., 2020).

The contribution of AS water to BoB OMZ will depend on the vertical mixing processes encountered by the northward-moving oxygenated HSC. Fig. 8 showed that net DO fluxes out of HSC due to turbulence is of $O(10^{-3}\text{--}10^{-2})$ $\mu\text{mol m}^{-2} \text{s}^{-1}$ and that due to salt fingering is of $O(10^{-2}\text{--}10^{-1})$ $\mu\text{mol m}^{-2} \text{s}^{-1}$. The contribution of DO fluxes is $\sim 0.01\text{--}0.1$ $\mu\text{mol kg}^{-1}$. There is seasonality in subsurface mixing within BoB; the vertical fluxes were weak in July and two orders of magnitude higher in September–October than in July (Cherian et al., 2020). This agrees with the increase in the contribution of vertical fluxes to OMZ towards the end of the year (Sarma, 2002). Moreover, the BoB receives high vertical organic matter fluxes due to river discharge increasing oxygen demand in subsurface layers (Ittekkot et al., 1991; Prakash et al., 2013). The decrease in DO due to the oxygen consumption rate in the subsurface (~ 81 Tg yr⁻¹) is around 1.72 $\mu\text{mol kg}^{-1}$ in 30-day period (Sarma, 2002). Thus, the contribution of the HSC in recharging the subsurface OMZ with DO depends on the variation in the distribution of high salinity water, vertical processes, and productivity in the BoB basin.

4. Summary and conclusions

Processes that can supply DO to BoB OMZ are of great interest owing to the curious capacity of the OMZ to stay above the tipping point (Bristow et al., 2017). Due to strong stratification in the northern BoB, recharging DO in the subsurface layers via air–sea interaction is highly improbable or extremely inefficient (D’Asaro et al., 2020). Cyclonic

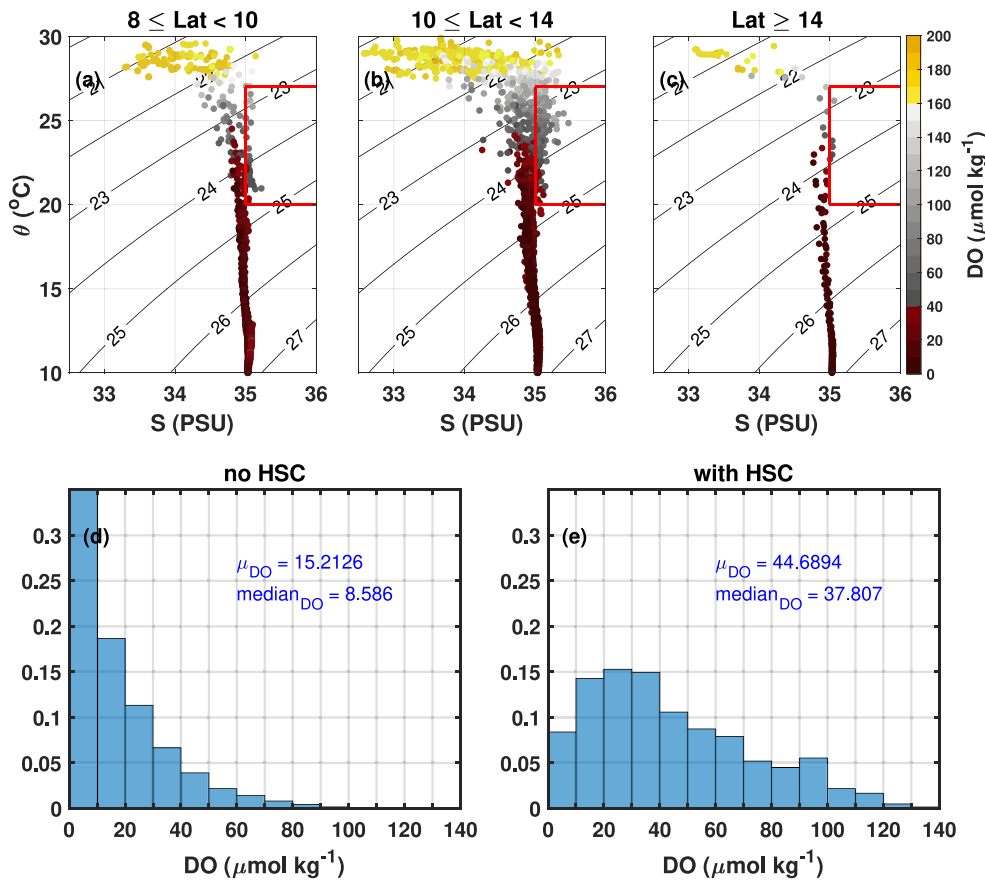


Fig. 10. (a)–(c) show θ -S diagram of Argo profiles like Fig. 7d. The latitudinal extent of Argo profiles within the BoB is mentioned at the top of each panel. The comparison of the normalized histogram of DO from Argo profiles identified (e) with HSC to DO from Argo profiles identified with (d) no HSC. The peak of the histogram with HSC has a higher DO than the peak of the histogram with no HSC. Mean (μ) and median DO are mentioned in blue.

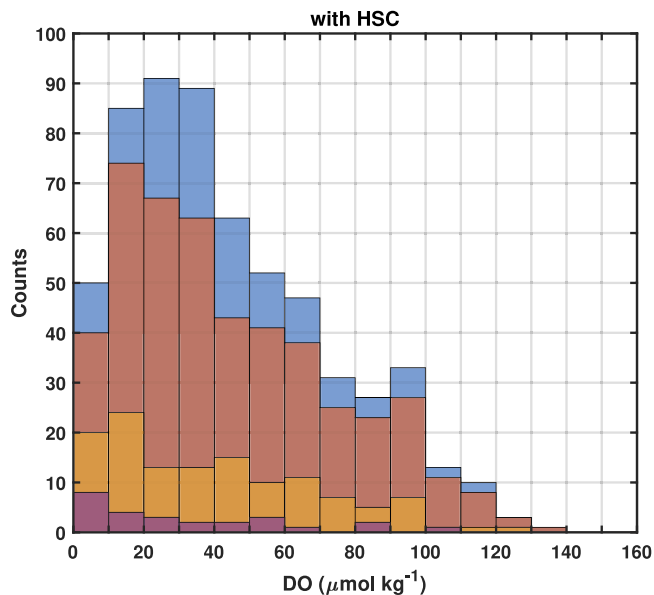


Fig. 11. Histogram of DO values within the HSC found in the Argo floats across the BoB. This is a decomposition of Fig. 10e with respect to the latitudes. Blue bars are the ones found between 8°–10° N. Brown bars show the counts of DO values found between 10°–12° N, and yellow bars show the points between 12°–14° N, and purple bars at the bottom show ones above 14° N.

eddies intensify OMZ in BoB through increased organic matter production, and anticyclonic eddies weaken the OMZ through ventilation of

DO into the OMZ in BoB (Sarma et al., 2018; Sarma and Udaya Bhaskar, 2018). A significant factor in controlling DO concentrations in the OMZ is the oxygen supply through the thermocline from layers above OMZ (Sarma, 2002). Replenishing these layers above BoB OMZ with DO is important for maintaining DO within OMZ (McCreary Jr. et al., 2013).

During the summer monsoon, SMC advects high salinity water from the AS into the BoB. Observations across the SMC in the southern BoB show that subsurface HSC is rich in DO (Fig. 7). Fig. 9a shows locations of Argo profiles throughout the BoB that carry TS signatures of HSC observed in the southern BoB. Salinity maxima within HSC are highest at the southern latitudes of BoB during July and decrease with an increase in time and latitude (Fig. 9b). These results suggest that HSC enters the southern BoB, moves northwards, and diffuses its salinity to the ambient lower salinity BoB water. HSC signatures from Argo profiles are scattered to the northern part of BoB, consistent with earlier reports (Singh et al., 2022). Apart from the in-situ data in southern BoB, profiles from Bio-Argo floats which have HSC also show higher DO than the ones which do not have HSC. The comparison between the profiles were carried out based on salinity values within the range of density values (Section 3.4) assuming HSC spreads spatially within the density layers and only diapycnal mixing processes responsible for cross-density DO transport. Estimates of turbulent and salt fingering fluxes for DO show that the HSC loses DO to layers below. The turbulent DO fluxes estimated in this study are comparable to average fluxes presented in Fischer et al. (2013), Brandt et al. (2015), but these studies did not consider salt fingering processes. Our analyses of *in situ* profiles show that the fluxes within the lower part of HSC are important to recharge the deeper BoB layers with HSC as a source of oxygen-rich water.

The results presented here are significant, given the long-term changes likely to manifest in the BoB. Some studies have suggested that streams like the Persian Gulf, which transports DO at depths of BoB OMZ (Jain et al., 2017; Sheehan et al., 2020), will weaken with changing climate, leading to the intensification of BoB OMZ (Laffoley and Baxter, 2019). Climate change will increase the stratification (Yamaguchi and Suga, 2019) and further restrict the vertical exchange of momentum. Lower vertical momentum exchange will reduce oxygen transfer from the mixed layer to deeper waters. Increased stratification will strengthen the barrier layer in the BoB; therefore, surface wind forcing will be ineffective in mixing DO to depths below the mixed layer. In such a scenario, horizontal transport of DO in subsurface layers will play an essential role in replenishing the DO values in subsurface layers, OMZ. The results suggest that SMC brings oxygen-rich high salinity water to the BoB at its southern end, and sub-basin scale circulation within BoB is responsible for the spread of this water into the BoB. Therefore, it is essential to study the impact of SMC on the subsurface DO in BoB using comprehensive observations and model simulations.

CRedit authorship contribution statement

Anoop A. Nayak: Writing – review & editing, Writing – original draft, Visualization, Methodology, Formal analysis, Conceptualization. **P.N. Vinayachandran:** Writing – review & editing, Writing – original draft, Supervision, Resources, Project administration, Data curation, Conceptualization. **Jenson V. George:** Data curation, Methodology, Writing – review & editing.

Declaration of competing interest

The authors declare that they have no known competing financial interests or personal relationships that could have appeared to influence the work reported in this paper.

Acknowledgements

The Ministry of Earth Sciences, the Government of India, funded the BoBBLE field program on board the R/V Sindhu Sadhana under its Monsoon Mission program administered by the Indian Institute of Tropical Meteorology, Pune. P.N.V. acknowledges partial financial support from the J C Bose fellowship provided by SERB, DST, Govt. of India. A.A.N. thanks Nihar Paul for his input in the Argo data analysis. Argo data were collected and made freely available by the International Argo Program and the national programs that contribute to it. (<https://argo.ucsd.edu>, <https://www.ocean-ops.org>). The Argo Program is part of the Global Ocean Observing System.

Data availability

The data for reproducing results of this work are available at <https://doi.org/10.5281/zenodo.7340408>. Argo data analysed in this study were obtained from <https://dataselection.euro-argo.eu/>. With the help of the website's data selection buttons and tabs, we selected Argo floats within the Bay of Bengal north of latitude, crossing the southern tip of Sri Lanka. The export option directs toward the download process.

References

- Al Azhar, M., Lachkar, Z., Lévy, M., Smith, S., 2017. Oxygen minimum zone contrasts between the Arabian Sea and the Bay of Bengal implied by differences in remineralization depth. *Geophys. Res. Lett.* 44 (21), 11–106. <http://dx.doi.org/10.1002/2017GL075157>.
- Argo, G., 2000. Argo float data and metadata from global data assembly centre (Argo GDAC). SEANOE.
- Bluteau, C.E., Jones, N.L., Ivey, G.N., 2011. Estimating turbulent kinetic energy dissipation using the inertial subrange method in environmental flows. *Limnol. Oceanography: Methods* 9 (7), 302–321. <http://dx.doi.org/10.4319/lom.2011.9.302>.
- Bluteau, C.E., Lueck, R.G., Ivey, G.N., Jones, N.L., Book, J.W., Rice, A.E., 2017. Determining mixing rates from concurrent temperature and velocity measurements. *J. Atmos. Ocean. Technol.* 34 (10), 2283–2293. <http://dx.doi.org/10.1175/JTECH-D-16-0250.1>.
- Brandt, P., Bange, H.W., Banyte, D., Dengler, M., Didwischus, S.-H., Fischer, T., Greatbatch, R.J., Hahn, J., Kanzow, T., Karstensen, J., et al., 2015. On the role of circulation and mixing in the ventilation of oxygen minimum zones with a focus on the eastern tropical North Atlantic. *Biogeosciences* 12 (2), 489–512. <http://dx.doi.org/10.5194/bg-12-489-2015>.
- Breitburg, D., Levin, L.A., Oschlies, A., Grégoire, M., Chavez, F.P., Conley, D.J., Garçon, V., Gilbert, D., Gutiérrez, D., Isensee, K., et al., 2018. Declining oxygen in the global ocean and coastal waters. *Science* 359 (6371), eaam7240. <http://dx.doi.org/10.1126/science.aam7240>.
- Bristow, L.A., Callbeck, C.M., Larsen, M., Altabet, M.A., Dekaezemacker, J., Forth, M., Gauns, M., Glud, R.N., Kuypers, M.M., Lavik, G., et al., 2017. N₂ production rates limited by nitrite availability in the Bay of Bengal oxygen minimum zone. *Nat. Geosci.* 10 (1), 24–29. <http://dx.doi.org/10.1038/ngeo2847>.
- Carpenter, J.H., 1965. The accuracy of the Winkler method for dissolved oxygen analysis 1. *Limnol. Oceanogr.* 10 (1), 135–140. <http://dx.doi.org/10.4319/lo.1965.10.1.0135>.
- Cherian, D., Shroyer, E., Wijesekera, H., Moum, J., 2020. The seasonal cycle of upper-ocean mixing at 8 N in the Bay of Bengal. *J. Phys. Oceanogr.* 50 (2), 323–342. <http://dx.doi.org/10.1175/JPO-D-19-0114.1>.
- Cullen, K., Shroyer, E.L., 2019. Seasonality and interannual variability of the Sri Lanka dome. *Deep. Sea Res. Part II: Top. Stud. Ocean.* 168, 104642. <http://dx.doi.org/10.1016/j.dsr2.2019.104642>.
- D'Asaro, E., Altabet, M., Kumar, N.S., Ravichandran, M., 2020. Structure of the Bay of Bengal oxygen deficient zone. *Deep. Sea Res. Part II: Top. Stud. Ocean.* 179, 104650. <http://dx.doi.org/10.1016/j.dsr2.2019.104650>.
- Fernández-Castro, B., Mouriño-Carballido, B., Benítez-Barrios, V., Chouciño, P., Fraile-Nuez, E., Graña, R., Piedeleu, M., Rodríguez-Santana, A., 2014. Microstructure turbulence and diffusivity parameterization in the tropical and subtropical Atlantic, Pacific and Indian Oceans during the Malaspina 2010 expedition. *Deep. Sea Res. Part I: Ocean. Res. Pap.* 94, 15–30. <http://dx.doi.org/10.1016/j.dsr.2014.08.006>.
- Fischer, T., Banyte, D., Brandt, P., Dengler, M., Krahmman, G., Tanhua, T., Visbeck, M., 2013. Diapycnal oxygen supply to the tropical North Atlantic oxygen minimum zone. *Biogeosciences* 10 (7), 5079–5093. <http://dx.doi.org/10.5194/bg-10-5079-2013>.
- George, J.V., Vinayachandran, P., Nayak, A.A., 2021. Enhanced double-diffusive salt flux from the high-salinity core of Arabian Sea origin waters to the Bay of Bengal. *J. Phys. Oceanogr.* 51 (2), 505–518. <http://dx.doi.org/10.1175/JPO-D-20-0192.1>.
- George, J.V., Vinayachandran, P., Vijith, V., Thushara, V., Nayak, A.A., Parganekar, S.M., Amol, P., Vijaykumar, K., Matthews, A.J., 2019. Mechanisms of barrier layer formation and erosion from in situ observations in the Bay of Bengal. *J. Phys. Oceanogr.* 49 (5), 1183–1200. <http://dx.doi.org/10.1175/JPO-D-18-0204.1>.
- Gordon, A.L., Shroyer, E.L., Mahadevan, A., Sengupta, D., Freilich, M., 2016. Bay of Bengal: 2013 northeast monsoon upper-ocean circulation. *Oceanography* 29 (2), 82–91. <http://dx.doi.org/10.5670/oceanog.2016.41>.
- Gordon, A.L., Shroyer, E., Murty, V., 2017. An Intrathermocline Eddy and a tropical cyclone in the Bay of Bengal. *Sci. Rep.* 7, 46218. <http://dx.doi.org/10.1038/srep46218>.
- Gregg, M.C., 1973. The microstructure of the ocean. *Sci. Am.* 228 (2), 64–77, URL <http://www.jstor.org/stable/24922981>.
- Gregg, M., D'Asaro, E., Riley, J., Kunze, E., 2018. Mixing efficiency in the ocean. *Annu. Rev. Mar. Sci.* 10, 443–473. <http://dx.doi.org/10.1146/annurev-marine-121916-063643>.
- Gruber, N., Sarmiento, J.L., 1997. Global patterns of marine nitrogen fixation and denitrification. *Glob. Biogeochem. Cycles* 11 (2), 235–266. <http://dx.doi.org/10.1029/97GB00077>.
- Hamilton, J.M., Lewis, M.R., Ruddick, B.R., 1989. Vertical fluxes of nitrate associated with salt fingers in the world's oceans. *J. Geophys. Research: Ocean.* 94 (C2), 2137–2145. <http://dx.doi.org/10.1029/JC094iC02p02137>.
- Howell, E.A., Doney, S.C., Fine, R.A., Olson, D.B., 1997. Geochemical estimates of denitrification in the Arabian Sea and the Bay of Bengal during WOCE. *Geophys. Res. Lett.* 24 (21), 2549–2552. <http://dx.doi.org/10.1029/97GL01538>.
- Ittekkot, V., Nair, R., Honjo, S., Ramaswamy, V., Bartsch, M., Manganini, S., Desai, B., 1991. Enhanced particle fluxes in Bay of Bengal induced by injection of fresh water. *Nature* 351 (6325), 385–387. <http://dx.doi.org/10.1038/351385a0>.
- Jain, V., Shankar, D., Vinayachandran, P., Kankonkar, A., Chatterjee, A., Amol, P., Almeida, A., Michael, G., Mukherjee, A., Chatterjee, M., et al., 2017. Evidence for the existence of Persian Gulf water and Red Sea water in the Bay of Bengal. *Clim. Dyn.* 48 (9), 3207–3226. <http://dx.doi.org/10.1007/s00382-016-3259-4>.
- Jensen, T.G., 2001. Arabian Sea and Bay of Bengal exchange of salt and tracers in an ocean model. *Geophys. Res. Lett.* 28 (20), 3967–3970. <http://dx.doi.org/10.1029/2001GL013422>.

- Johnson, K.S., Riser, S.C., Ravichandran, M., 2019. Oxygen variability controls denitrification in the Bay of Bengal oxygen minimum zone. *Geophys. Res. Lett.* 46 (2), 804–811. <http://dx.doi.org/10.1029/2018GL079881>.
- Kara, A.B., Rochford, P.A., Hurlburt, H.E., 2000. Mixed layer depth variability and barrier layer formation over the North Pacific Ocean. *J. Geophys. Research: Ocean.* 105 (C7), 16783–16801. <http://dx.doi.org/10.1029/2000JC900071>.
- Keeling, R.F., Garcia, H.E., 2002. The change in oceanic O₂ inventory associated with recent global warming. *Proc. Natl. Acad. Sci.* 99 (12), 7848–7853. <http://dx.doi.org/10.1073/pnas.122154899>.
- Kumar, S.P., Nuncio, M., Ramaiah, N., Sardesai, S., Narvekar, J., Fernandes, V., Paul, J.T., 2007. Eddy-mediated biological productivity in the Bay of Bengal during fall and spring intermonsoons. *Deep. Sea Res. Part I: Ocean. Res. Pap.* 54 (9), 1619–1640. <http://dx.doi.org/10.1016/j.dsr.2007.06.002>.
- Lachkar, Z., 2020. Climatic control of regional ocean deoxygenation: insights from recent trends in the north Indian Ocean. In: *Ocean Sciences Meeting 2020*. AGU.
- Laffoley, D., Baxter, J.M., 2019. Ocean deoxygenation: Everyone's problem-Causes, impacts, consequences and solutions. IUCN Gland, <http://dx.doi.org/10.2305/IUCN.CH.2019.13.en>.
- Le Moigne, F.A., Gallinari, M., Laurenceau, E., de La Rocha, C.L., 2013. Enhanced rates of particulate organic matter remineralization by microzooplankton are diminished by added ballast minerals. *Biogeosciences* 10 (9), 5755–5765. <http://dx.doi.org/10.5194/bg-10-5755-2013>.
- McCreary Jr., J.P., Yu, Z., Hood, R.R., Vinayachandran, P., Furue, R., Ishida, A., Richards, K.J., 2013. Dynamics of the Indian-Ocean oxygen minimum zones. *Prog. Oceanogr.* 112, 15–37. <http://dx.doi.org/10.1016/j.pocean.2013.03.002>.
- Nayak, A.A., Vinayachandran, P.N., George, J.V., 2022. Turbulent dissipation rates across the Summer Monsoon Current. *Ocean. Dyn.* 72 (9), 695–714. <http://dx.doi.org/10.1007/s10236-022-01524-w>.
- Oakey, N., 1985. Statistics of mixing parameters in the upper ocean during JASIN phase 2. *J. Phys. Oceanogr.* 15 (12), 1662–1675. [http://dx.doi.org/10.1175/1520-0485\(1985\)015<1662:SOMPIT>2.0.CO;2](http://dx.doi.org/10.1175/1520-0485(1985)015<1662:SOMPIT>2.0.CO;2).
- Osborn, T.R., 1980. Estimates of the local rate of vertical diffusion from dissipation measurements. *J. Phys. Oceanogr.* 10 (1), 83–89. [http://dx.doi.org/10.1175/1520-0485\(1980\)010<0083:EOTLRO>2.0.CO;2](http://dx.doi.org/10.1175/1520-0485(1980)010<0083:EOTLRO>2.0.CO;2).
- Osborn, T.R., Cox, C.S., 1972. Oceanic fine structure. *Geophys. Astrophys. Fluid Dyn.* 3 (1), 321–345. <http://dx.doi.org/10.1080/03091927208236085>.
- Oschlies, A., Brandt, P., Stramma, L., Schmidtko, S., 2018. Drivers and mechanisms of ocean deoxygenation. *Nat. Geosci.* 11 (7), 467–473. <http://dx.doi.org/10.1038/s41561-018-0152-2>.
- Paulmier, A., Ruiz-Pino, D., 2009. Oxygen minimum zones (OMZs) in the modern ocean. *Prog. Oceanogr.* 80 (3–4), 113–128. <http://dx.doi.org/10.1016/j.pocean.2008.08.001>.
- Prakash, S., Prakash, P., Ravichandran, M., 2013. Can oxycline depth be estimated using sea level anomaly (SLA) in the northern Indian Ocean? *Remote. Sens. Lett.* 4 (11), 1097–1106. <http://dx.doi.org/10.1080/2150704X.2013.842284>.
- Rao, C., Naqvi, S., Kumar, M.D., Varaprasad, S., Jayakumar, D., George, M., Singbal, S., 1994. Hydrochemistry of the Bay of Bengal: possible reasons for a different water-column cycling of carbon and nitrogen from the Arabian Sea. *Mar. Chem.* 47 (3–4), 279–290. [http://dx.doi.org/10.1016/0304-4203\(94\)90026-4](http://dx.doi.org/10.1016/0304-4203(94)90026-4).
- Rath, S., Vinayachandran, P., Behara, A., Neema, C., 2019. Dynamics of summer monsoon current around Sri Lanka. *Ocean. Dyn.* 69 (10), 1133–1154. <http://dx.doi.org/10.1007/s10236-019-01295-x>.
- Rixen, T., Cowie, G., Gaye, B., Goes, J., do Rosário Gomes, H., Hood, R.R., Lachkar, Z., Schmidt, H., Segsneider, J., Singh, A., 2020. Reviews and syntheses: Present, past, and future of the oxygen minimum zone in the northern Indian Ocean. *Biogeosciences* 17 (23), 6051–6080. <http://dx.doi.org/10.5194/bg-17-6051-2020>.
- Roy, R., Vinayachandran, P., Sarkar, A., George, J., Parida, C., Lotliker, A., Prakash, S., Choudhury, S.B., 2021. Southern Bay of Bengal: A possible hotspot for CO₂ emission during the summer monsoon. *Prog. Oceanogr.* 197, 102638. <http://dx.doi.org/10.1016/j.pocean.2021.102638>.
- Ruddick, B., 1983. A practical indicator of the stability of the water column to double-diffusive activity. *Deep. Sea Res. Part A. Ocean. Res. Pap.* 30 (10), 1105–1107. [http://dx.doi.org/10.1016/0198-0149\(83\)90063-8](http://dx.doi.org/10.1016/0198-0149(83)90063-8).
- Sarma, V., 2002. An evaluation of physical and biogeochemical processes regulating the oxygen minimum zone in the water column of the Bay of Bengal. *Glob. Biogeochem. Cycles* 16 (4), 46–146–10. <http://dx.doi.org/10.1029/2002GB001920>.
- Sarma, V., Jagadeesan, L., Dalabehera, H., Rao, D., Kumar, G., Durgadevi, D., Yadav, K., Behera, S., Priya, M., 2018. Role of eddies on intensity of oxygen minimum zone in the Bay of Bengal. *Cont. Shelf Res.* 168, 48–53. <http://dx.doi.org/10.1016/j.csr.2018.09.008>.
- Sarma, V., Rao, G., Viswanadham, R., Sherin, C., Salisbury, J., Omand, M.M., Mahedevan, A., Murty, V., Shroyer, E.L., Baumgartner, M., et al., 2016. Effects of freshwater stratification on nutrients, dissolved oxygen and phytoplankton in the Bay of Bengal. *Oceanography* 29 (2), 222–231. <http://dx.doi.org/10.5670/oceanog.2016.54>.
- Sarma, V., Udaya Bhaskar, T., 2018. Ventilation of oxygen to oxygen minimum zone due to anticyclonic eddies in the Bay of Bengal. *J. Geophys. Research: Biogeosciences* 123 (7), 2145–2153. <http://dx.doi.org/10.1029/2018JG004447>.
- Sharples, J., Coates, M.J., Sherwood, J.E., 2003. Quantifying turbulent mixing and oxygen fluxes in a Mediterranean-type, microtidal estuary. *Ocean. Dyn.* 53 (3), 126–136. <http://dx.doi.org/10.1007/s10236-003-0037-8>.
- Sheehan, P.M., Webber, B.G., Sanchez-Franks, A., Matthews, A.J., Heywood, K.J., Vinayachandran, P., 2020. Injection of oxygenated Persian Gulf Water into the southern Bay of Bengal. *Geophys. Res. Lett.* 47 (14), <http://dx.doi.org/10.1029/2020GL087773>, e2020GL087773.
- Singh, U., Dhipu, T., Vinayachandran, P., Natarajan, V., 2022. Front and skeleton features based methods for tracking salinity propagation in the ocean. *Comput. Geosci.* 159, 104993. <http://dx.doi.org/10.1016/j.cageo.2021.104993>.
- Singh, A., Gandhi, N., Ramesh, R., Prakash, S., 2015. Role of cyclonic eddy in enhancing primary and new production in the Bay of Bengal. *J. Sea Res.* 97, 5–13. <http://dx.doi.org/10.1016/j.seares.2014.12.002>.
- St. Laurent, L., Schmitt, R.W., 1999. The contribution of salt fingers to vertical mixing in the North Atlantic Tracer Release Experiment. *J. Phys. Oceanogr.* 29 (7), 1404–1424. [http://dx.doi.org/10.1175/1520-0485\(1999\)029<1404:TCOSFT>2.0.CO;2](http://dx.doi.org/10.1175/1520-0485(1999)029<1404:TCOSFT>2.0.CO;2).
- Stramma, L., Johnson, G.C., Sprintall, J., Mohrholz, V., 2008. Expanding oxygen-minimum zones in the tropical oceans. *Science* 320 (5876), 655–658. <http://dx.doi.org/10.1126/science.1153847>.
- Sverdrup, H., 1938. On the explanation of the oxygen minima and maxima in the oceans. *ICES J. Mar. Sci.* 13 (2), 163–172. <http://dx.doi.org/10.1093/icesjms/13.2.163>.
- Vinayachandran, P., Masumoto, Y., Mikawa, T., Yamagata, T., 1999. Intrusion of the southwest monsoon current into the Bay of Bengal. *J. Geophys. Research: Ocean.* 104 (C5), 11077–11085. <http://dx.doi.org/10.1029/1999JC900035>.
- Vinayachandran, P., Masumoto, Y., Roberts, M., Hugget, J., Halo, I., Chatterjee, A., Amol, P., Gupta, G.V., Singh, A., Mukherjee, A., et al., 2021. Reviews and syntheses: Physical and biogeochemical processes associated with upwelling in the Indian Ocean. *Biogeosciences Discuss.* 1–128. <http://dx.doi.org/10.5194/bg-18-5967-2021>.
- Vinayachandran, P., Matthews, A.J., Vijay Kumar, K., Sanchez-Franks, A., Thushara, V., George, J., Vijith, V., Webber, B.G., Queste, B.Y., Roy, R., et al., 2018. BoBBLE (Bay of Bengal Boundary Layer Experiment): Ocean-atmosphere interaction and its impact on the South Asian monsoon. *Bull. Am. Meteorol. Soc.* 99 (8), 1569–1587. <http://dx.doi.org/10.1175/BAMS-D-16-0230.1>.
- Vinayachandran, P., Shankar, D., Vernekar, S., Sandeep, K., Amol, P., Neema, C., Chatterjee, A., 2013. A summer monsoon pump to keep the Bay of Bengal salty. *Geophys. Res. Lett.* 40 (9), 1777–1782. <http://dx.doi.org/10.1002/grl.50274>.
- Vinayachandran, P., Yamagata, T., 1998. Monsoon response of the sea around Sri Lanka: generation of thermal domes and anticyclonic vortices. *J. Phys. Oceanogr.* 28 (10), 1946–1960. [http://dx.doi.org/10.1175/1520-0485\(1998\)028<1946:MRO TSA>2.0.CO;2](http://dx.doi.org/10.1175/1520-0485(1998)028<1946:MRO TSA>2.0.CO;2).
- Vos, A.d., Pattiaratchi, C., Wijeratne, E., 2014. Surface circulation and upwelling patterns around Sri Lanka. *Biogeosciences* 11 (20), 5909–5930. <http://dx.doi.org/10.5194/bg-11-5909-2014>.
- Webber, B.G., Matthews, A.J., Vinayachandran, P., Neema, C., Sanchez-Franks, A., Vijith, V., Amol, P., Baranowski, D.B., 2018. The dynamics of the Southwest Monsoon current in 2016 from high-resolution in situ observations and models. *J. Phys. Oceanogr.* 48 (10), 2259–2282. <http://dx.doi.org/10.1175/JPO-D-17-0215.1>.
- Wyrtki, K., 1962. The oxygen minima in relation to ocean circulation. In: *Deep Sea Research and Oceanographic Abstracts*. vol. 9, Elsevier, pp. 11–23. [http://dx.doi.org/10.1016/0011-7471\(62\)90243-7](http://dx.doi.org/10.1016/0011-7471(62)90243-7).
- Yamaguchi, R., Suga, T., 2019. Trend and variability in global upper-ocean stratification since the 1960s. *J. Geophys. Research: Ocean.* 124 (12), 8933–8948. <http://dx.doi.org/10.1029/2019JC015439>.